



SELECTIVE ELECTROCHEMICAL REDUCTION OF CO₂ TO HIGH VALUE CHEMICALS

Grant agreement no.: 851441

Start date: 01.01.2020 – **Duration:** 36 months

Project Coordinator: Dr. Brian Seger - DTU

DELIVERABLE REPORT

D.7.2 – DEVELOPED PORE-LEVEL TRANSPORT MODEL		
Due Date	31 January 2022	
Author (s)	Etienne Boutin, Shuo Liu, Francesca Lorenzutti, Sophia Haussener	
Workpackage	WP 7	
Workpackage Leader	EPFL	
Lead Beneficiary	EPFL	
Date released by WP leader	21/01/2022	
Date released by Coordinator	22/01/2022	
DISSEMINATION LEVEL		
PU	Public	X
PP	Restricted to other programme participants (including the Commission Services)	
RE	Restricted to a group specified by the consortium (including the Commission Services)	
CO	Confidential, only for members of the consortium (including the Commission Services)	
NATURE OF THE DELIVERABLE		
R	Report	X
P	Prototype	
D	Demonstrator	
O	Other	

SUMMARY	
Keywords	<i>Pore-level; Mass transport; CO₂ reduction; Modeling</i>
Abstract	<p><i>The deliverable reports on the development of pore-level models for mass transport that provide better representation of the phenomena involved at this scale. The pore-level model has been developed and initially applied in a well-defined silver electrode porous structure (namely a silver reverse opal structure made of overlapping spheres of known radius). This method allows to restrict the study to a small size representative domain due to the high degree of symmetry in the plane of the electrode. Using the bulk concentration and the potential dependence of the current at both ends of the model, the diffusion-reaction (bulk and electrode) model is solved for. This model provides space-dependent concentration and as a consequence a space dependent current density for CO production and the competing H₂ production. This first version of the model has been validated with a set of experimental data. Further extension of this model are presented. They account for migration effects on charged species in the double layer region where the electric field is important. The adsorption-desorption transport phenomena of carbon monoxide product are also considered in a subsequent extension and its effect on the catalytic rate is also accounted for. Furthermore, a tomography-based method to quantify the effective transport in the complex porous structure of the GDL and the catalyst layer is introduced.</i></p>
Public abstract for confidential deliverables	<i>NONE – deliverable is public</i>

REVISIONS			
Version	Date	Changed by	Comments
0.1	13/12/2021	Etienne Boutin	
0.2	21/01/2022	Sophia Haussener	

REPORTS ON DEVELOPED PORE-LEVEL TRANSPORT MODEL

CONTENT

1	Introduction	4
2	Pore-level model for well-defined structures.....	4
2.1.	Methodology	4
2.2.	Governing Equations	5
2.3.	Validation	6
3	Definition of kinetic parameters with butler-volmer relationship	7
3.1	Methodology	7
3.2	Governing equations	7
3.3	Validation.....	7
4	Inclusion of double layer migration effects	8
4.1.	Methodology	8
4.2.	Governing equations	9
4.3.	Results and Validation	10
5	Inclusion of product adsorption-desorption phenomena	11
5.1.	Methodology	11
5.2.	Governing equations	12
5.3.	Validation	13
6	Tomography-based modeling	13
6.1.	Methodology	14
6.2.	Sample characterization.....	17
6.3.	Results	17
7	Conclusions	20
8	References	20

1 INTRODUCTION

Upscaling the CO₂ electrochemical reduction reaction (CO₂RR) and its implementation in practical devices requires the use of device and electrode designs that are able to operate at large current densities. Due to the limited solubility of CO₂ in water, approaches to reduce the transport path to the catalytic site and to increase the active surface of the electrode/electrolyte are required, such as the introduction of porous electrodes (termed gas diffusion electrodes – GDEs) where CO₂ is fed either by a flowing catholyte or by a gaseous stream. In such a configuration, the concentration of reactant and product, the potential and the partial current densities are much more heterogeneous than in a flat electrode configuration. This inhomogeneity is due to coupled mass transport of the various involved species in the complex porous structure of the electrode layer(s). In this deliverable, we summarize a variety of newly developed models that take into consideration the detailed mass and charge transport at the interface, in the electric double layer, in the diffusion layer and in the complex porous structure. The models provide spatially resolved current density as a function of spatially resolved concentrations.

We consider a concentration corrected Butler-Volmer like relationship between potential and current density of a given reaction. We then provide additional features that can refine the initial model by considering the effect of charge accumulation in the double layer region, resulting in important electrostatic field under operation. We also provide means to correct the intensity of the predicted current by taking into account the adsorption of some product that compete with the adsorption of reaction intermediates. Finally, we detail the strategy to transpose such a model into a realistic and complex electrode structure. This approach utilizes nano-tomography analysis and segmentation procedures to digitalize the exact geometry that is subsequently used in direct pore-level simulations.

2 PORE-LEVEL MODEL FOR WELL-DEFINED STRUCTURES

2.1. Methodology

An initial model was developed before the start of SelectCO₂ and builds the basis for the subsequent pore-level models. The method and governing equations are introduced here and follow [1]. This initial pore-level model was developed in relation with and validated by an important set of experimental data established by Surendranath et al. [2] on well-defined porous silver structures. These structures are an ordered silver inverse opal electrode structure fabricated by using highly monodisperse, 200 nm diameter polystyrene spheres to create a well defined face centered cubic (FCC) lattice on top of an electrode, onto which silver is then electrodeposited and afterwards the polystyrene spheres are dissolved in organics solvent. By increasing the electrodeposition time, the thickness of the nanostructure was increased and various thicknesses were compared with a flat silver electrode surface for CO₂ electrochemical reduction performance in 0.1M KHCO₃ electrolyte. The effect of the nanostructure was investigated on roughness factor (RF) ranging from 4 to 109 and showed enhanced performances and selectivity at high roughness factor. Thanks of the high symmetry of the pattern, it is possible to represent the structure by a representative domain depicted in Fig. 1. This domain can be replicated in the z-direction to account for the varying thickness of the films while maintaining the symmetry condition of the lateral walls.

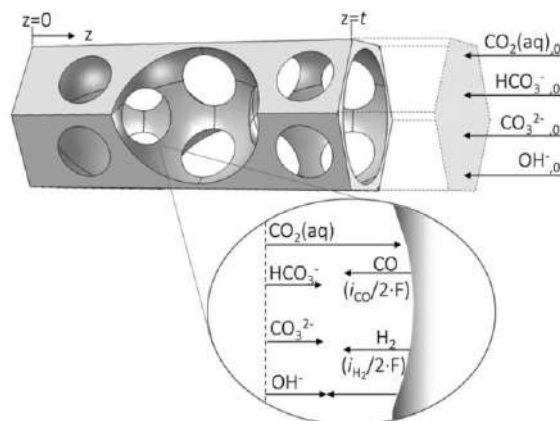


Figure 1. Illustration of the representative domain used for the pore-level model [1].

2.2. Governing Equations

2.1.1 Boundary conditions

- The bottom of the model (left side in Fig.1), connected to the electrode, has a no flow condition.
- The lateral walls of the domain are chosen to be the symmetric plane of the FCC lattice so symmetry conditions apply for species fluxes:

$$\mathbf{J}_i \cdot \mathbf{n} = 0 \quad (\text{Eq. 1})$$

where \mathbf{J}_i is the flux vector of species i and \mathbf{n} is the normal vector.

- At the other end of the domain, the porous electrode/electrolyte interface is followed by a pure electrolyte domain of thickness $1 \mu\text{m}$ to account for the presence of the diffusion boundary layer. At the extremity of this boundary layer (right side in Fig.1) a concentration condition is applied to equal the bulk concentration of 0.1M KHCO_3 electrolyte saturated with CO_2 .

Table 1. Species bulk concentrations in 0.1 K KHCO_3 at 25°C .

$\text{CO}_{2,\text{aq}}$ [M]	HCO_3^- [M]	CO_3^{2-} [M]	OH^- [M]
0.033	0.1	$2.9 \cdot 10^{-5}$	$6.6 \cdot 10^{-8}$

2.1.2 Homogeneous diffusion – reactions

The model assumed neither convection nor migration in the first place (see later sections for the corresponding improvements) in the porous structure, with mass balanced being governed by a diffusion-reaction equation.

$$\frac{dC_i}{dt} = D_i \nabla^2 C_i - R_i \quad (\text{Eq. 2})$$

Diffusion coefficient for each species are taken from literature. Buffer reaction of the CO_2 -bicarbonate-carbonate system in alkaline solution are considered:



These reactions are considered as reversible so that both forward and backward rate constants are computed rather than imposing the equilibrium.

2.1.3 Heterogeneous reactions

The specificity of the pore-level model is that the modelled electrode-electrolyte interface is not a flat surface but a 3D surface defined by the FCC lattice. At all points of the interface a Butler-Volmer like expression is set as electrochemical reaction for both CO and H_2 production:

$$j_{\text{CO}} = j_{0,\text{CO}} \left(\frac{C_{\text{CO}_3^{2-}}}{C_{\text{CO}_3^{2-},0}} \right)^m \left(\frac{C_{\text{OH}^-}}{C_{\text{OH}^-,0}} \exp\left(\frac{\alpha_{a,\text{CO}} F \eta}{RT}\right) - \frac{C_{\text{CO}_2}}{C_{\text{CO}_2,0}} \exp\left(-\frac{\alpha_{c,\text{CO}} F \eta}{RT}\right) \right) \quad (\text{Eq. 5})$$

$$j_{\text{H}_2} = j_{0,\text{H}_2} \left(\frac{C_{\text{OH}^-,0}}{C_{\text{OH}^-}} \right)^n \left(\frac{C_{\text{OH}^-}}{C_{\text{OH}^-,0}} \exp\left(\frac{\alpha_{a,\text{H}_2} F \eta}{RT}\right) - \exp\left(-\frac{\alpha_{c,\text{H}_2} F \eta}{RT}\right) \right) \quad (\text{Eq. 6})$$

Where j_0 stands for exchange current density, α_a and α_c are anodic and cathodic transfer coefficients, respectively, and 0 subscript on concentration terms refers to the local concentration at the electrode/electrolyte interface. For both reactions a limiting current was extracted from experimental data and integrated in the model as:

$$i = \frac{i_w}{\left|1 + \frac{i_w}{i_{lim}}\right|} \quad (\text{Eq. 7})$$

2.3. Validation

All differential and algebraic equations were solved on a 3D tetrahedral mesh using a finite element solver (COMSOL 5.3). Following parameters were fitted to the experimental data in order to minimize the sum of square errors (SSE) between the model and the experimental data for a roughness factor (RF) equals to 4 (this roughness factor is the one measured for a flat Ag surface). Fitted parameters are shown in Table 2 for two sets of data. In the first one m and n values have been taken as 1. In the second set, m and n have been allowed to be higher than one and considered to be 1.2.

Table 2. Empirical parameters fitted to the experimental data of a planar Ag electrode. R^2 quantified the goodness of fit for both sets. Where $\alpha_c = \beta$ and $\alpha_a = 2 - \beta$.

Set	$i_{0,CO}$ [mA cm ⁻²]	i_{0,H_2} [mA cm ⁻²]	$i_{lim,CO}$ [mA cm ⁻²]	i_{lim,H_2} [mA cm ⁻²]	β_{CO}	β_{H_2}	m	n	R_{CO}^2 [%]	$R_{H_2}^2$ [%]
1	$1.0012 \cdot 10^{-5}$	$7.0102 \cdot 10^{-10}$	0.4	1.1	0.29	0.95	1	1	71	68
2	$8.4083 \cdot 10^{-6}$	$9.2084 \cdot 10^{-10}$	0.4	1.1	0.29	0.95	1.2	1.2	81	79

When the model was extended to higher RF with the parameter fitted for a RF of 4, the simulated performances were in good agreement with the experimental data as pictured in Fig. 2, validating the model.

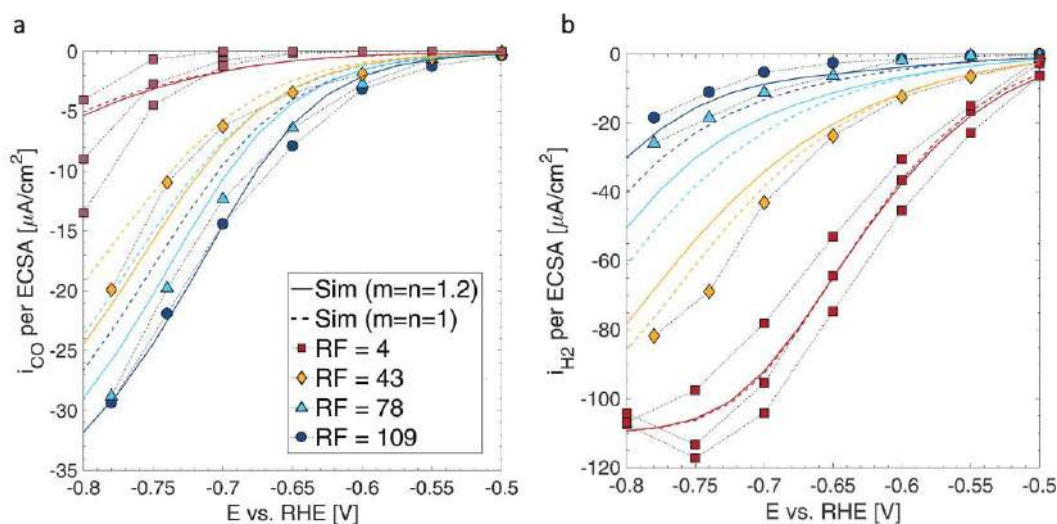


Figure 2. Partial current density of a) CO and b) H₂ for the CO₂ and water reduction reactions, normalized by the electrochemical active surface area (ECSA) [1]. The experimental data from Yoon et al. [2] is shown with markers. The computed results are shown with a dashed ($m = n = 1$) and a solid line ($m = n = 1.2$). The lines and markers are color coded based on their roughness factor RF.

The validated model can then be used to investigate various electrode thicknesses and other electrode geometries (changing sphere radius, porosity, etc.) in order to guide pore-geometry optimization. We observed a higher Faradaic efficiency for CO as the thickness increases and the sphere radius decreases. Considering that larger electrode thicknesses induce reduced mass transfer, resulting in better Faradaic efficiency towards CO, we proposed the introduction of an inert porous top layer on top of the silver porous electrode to further increase the performance. This additional, inert layer serves as a transport buffering layer and simulations indicated that a doubling in the Faradaic efficiency could be obtained.

In the next sections we will present several phenomena that can be added to this initial model to better take into account the migration effect on the double layer along with competitive adsorption of species at the active sites or the exact geometry of morphologically more complex porous electrode structures.

3 DEFINITION OF KINETIC PARAMETERS WITH BUTLER-VOLMER RELATIONSHIP

One of the most sensible aspects in modeling CO₂ electrochemical reduction is to capture the interfacial relationship between potential, concentrations and current densities. The definition of such parameters usually also involves mass transport models but in a reverse manner where mass transport is made really simple to model. Usually, related experiments are conducted in an H-cell with a flat electrode. In such experiments, one obtains a uniform and easy to compute (from partial current densities) concentration of species enabling the fit of a modeled current-potential-concentrations relationship. Most of the models so far are considering a Butler-Volmer like equation to capture this interfacial relationship. We present here such strategy applied to SelectCO2 partner experimental dataset and also emphasize its limitation, requiring the adaptation presented in section 4 and 5.

3.1 Methodology

The estimation of interfacial concentration of species considers a Nernst boundary layer of a defined thickness δ , present when experiments are performed at a flat electrode in an H-cell. Such a model considers the surface of the electrode as flat and much larger than the boundary layer thickness, reducing the problem to 1D without convection inside the Nernst boundary layer, while infinite convection is considered right outside this boundary.

3.2 Governing equations

3.2.1 Boundary conditions

At the electrode ($x=0$), a no flux condition is applied. Because convection is considered as infinite outside the Nernst boundary layer, all concentrations are considered equal to the bulk at this position ($x=\delta$), i.e. $C_{i, x=\delta} = C_{i, \text{bulk}}$.

3.2.2 Homogeneous diffusion – reactions

Diffusion-reaction equations (identical as described in section 2.1.2) are solved for in the Nernst boundary layer.

3.2.3 Heterogeneous reactions

For the heterogeneous reaction, the following relations are considered:

$$j_{CO} = -j_{0,CO} \left(\frac{C_{CO_3^{2-}}}{C_{CO_3^{2-},0}} \right) \exp\left(-\frac{\alpha_{c,CO} F \eta}{RT}\right) \quad (\text{Eq. 8})$$

$$j_{H_2} = -j_{0,H_2,A} \left(\frac{C_{H^+}}{C_{H^+,0}} \right) \exp\left(\frac{\alpha_{c,H_2,A} F \eta}{RT}\right) - j_{0,H_2,B} \exp\left(\frac{\alpha_{c,H_2,B} F \eta}{RT}\right) \quad (\text{Eq. 9})$$

In Eq. 9, the subscript A (“Acid”) stands for reduction of protons (eq. 10) and subscript B (“Base”) stands for reduction of water (Eq. 11).



In such a simple H-cell configuration, CO₂ electrochemical reduction data are collected, interfacial concentrations are solved for, and only j_0 and α coefficient are fitted to approach experimental data points.

3.3 Validation

SELECTCO2 partner TUB realized a series of experiments in an H-cell and a silver-based catalyst that they prepared. The application of the above-mentioned method to this set of data, enabled a quite exact fit of the CO partial current density as can be observed on Figure 3a.

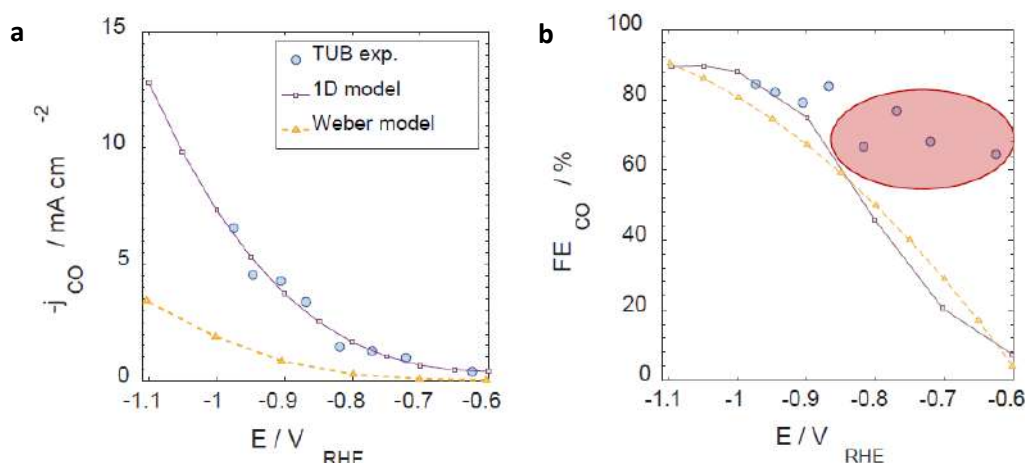


Figure 3. a) Partial current density for CO production at a flat silver electrode experimentally determined by TUB (blue circles), modeled following Weber kinetic parameters (yellow triangles) and modeled following our adjusted kinetics parameters (purple squares). b) CO Faradaic efficiency in the same conditions as in a). Region of mismatch between model and experiment are highlighted by the red circle.

Nevertheless, to obtain this fit, an adjustment of the kinetics parameter previously established by Weber *et al.* [3] was necessary as detailed in Table 3. Additionally, the Faradaic efficiency for CO, that is well represented by the model at more cathodic potential, is less well predicted by the model at less cathodic potential as highlighted by the red circle in Figure 3b). This observation also highlights the limitation of a simple Butler-Volmer like representation of kinetic behavior as other phenomena such as electrostatic field effect of catalytic site inhibition by the products are taking place. The integration of these phenomena into the model previously established is the object of section 5.

Table 3. Empirical parameters fitted to the experimental data of a planar Ag electrode.

Model	$i_{0,H_2,A}$ [mA cm ⁻²]	$\alpha_{c,H_2,A}$	$i_{0,H_2,B}$ [mA cm ⁻²]	$\alpha_{c,H_2,B}$	$i_{0,CO}$ [mA cm ⁻²]	$\alpha_{c,CO}$
Weber	9.79×10^{-4}	0.27	1.16×10^{-6}	0.36	4.71×10^{-4}	0.44
EPFL	1.21×10^{-3}	0.25	2.57×10^{-6}	0.34	5.21×10^{-3}	0.40

4 INCLUSION OF DOUBLE LAYER MIGRATION EFFECTS

In this chapter, we add convection and migration phenomena to the model by developing a complete electrical double layer model.

Since the hydrogen evolution reaction (HER) dominates in acidic solutions, CO₂ reduction process is traditionally conducted in an alkaline or near neutral medium. [4] This is also the case in SELECTCO₂, for example with the H-cell, which is operated in a near neutral environment (KHCO₃ solution). However, the reaction of CO₂ with hydroxide to generate carbonate in near neutral media fundamentally limits the conversion and product-specific efficiency of CO₂ reduction. [5,6] Gu *et al.* showed that by suppressing the predominant HER using alkali cations, CO₂ reduction can be conducted in acidic medium, therefore overcoming the carbonate problem. [7] Enticed by this observation, we chose for an application of the electrical double layer model an acidic environment and a rotating disc electrode experiment. We will show that the CO₂ reduction reaction in acidic electrolyte can be promoted while the undesired HER can be suppressed by the presence of alkali cations.

4.1. Methodology

The double layer model was based on solving the Poisson-Nernst-Planck (PNP) equations. The model accounts for diffusion, convection and migration as mass transport mechanisms. The ions H⁺, K⁺ and OTf⁻ ions were considered.

The reduction of H^+ ions was regarded as the only source of HER in strongly acidic media. [7] The model domain includes the Stern layer, the diffuse/diffusion layer, and the bulk electrolyte region as shown in Figure 4.

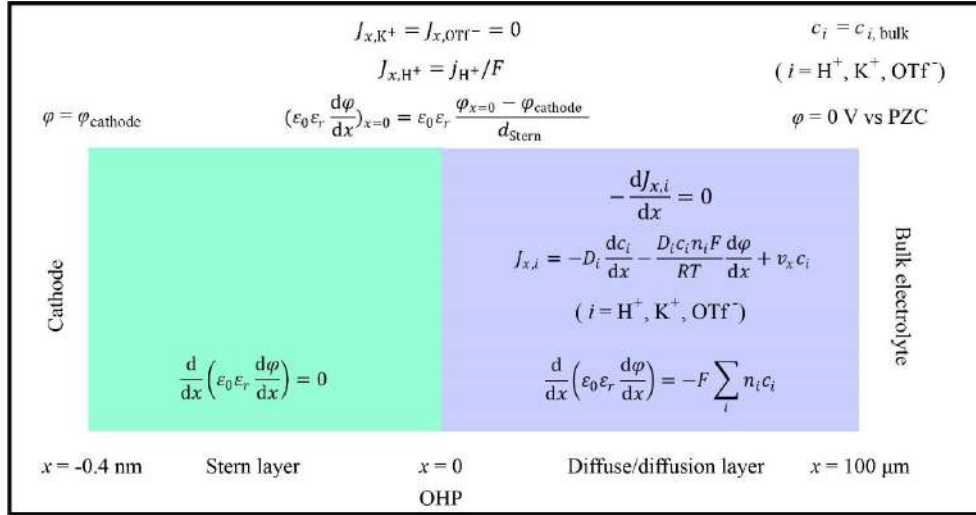


Figure 4. Governing equations and boundary conditions used for the 1-dimensional simulation. From left to right: the cathode, the Stern layer, the diffuse/diffusion layer, and the bulk electrolyte region. OHP is used as origin ($x=0$). [7]

4.2. Governing equations

The Poisson-Nernst-Planck equations at steady state are solved in the region between outer Helmholtz plane (OHP) and bulk electrolyte:

$$\frac{\partial c_i}{\partial t} = -\frac{\partial J_{x,i}}{\partial x} = 0 \quad (\text{Eq. 12})$$

$$J_{x,i} = -D_i \frac{dc_i}{dx} - \frac{D_i c_i n_i F}{RT} \frac{d\varphi}{dx} + v_x c_i \quad (\text{Eq. 13})$$

where c_i is the concentration of species i (with $i = K^+, H^+$ and OTf^-), D_i is the diffusion coefficient of species i , n_i is the charge of species i , R is the ideal gas constant, T is the temperature, φ is the potential and v_x is the velocity of solution in x -direction. For a rotating disk electrode, the velocity in axial direction at different x -locations can be estimated as:

$$v_x = -0.51x^2 \sqrt{\frac{\omega^3}{\nu}} \quad (\text{Eq. 14})$$

where ω is the rotation speed (unit: rad/s) of the disk electrode, ν is the kinematic viscosity of water. The Poisson equation is used to calculate the potential change, given by:

$$\frac{d}{dx}(\epsilon_0 \epsilon_r \frac{d\varphi}{dx}) = -F \sum_i n_i c_i \quad (\text{Eq. 15})$$

where ϵ_0 is the permittivity of vacuum and ϵ_r is the relative permittivity of water. The boundary conditions for the domain between OHP and bulk electrolyte are given by: At the right side ($x = 100 \text{ μm}$), the concentration of each species equals to the bulk concentration of this species, and the potential equals to 0 V vs PZC (potential of zero charge). At the left side ($x = 0$), the flux of each species was given as:

$$J_{x,K^+} = J_{x,OTf^-} = 0 \quad (\text{Eq. 16})$$

$$J_{x,H^+} = \frac{j_{H^+}}{F} \quad (\text{Eq. 17})$$

where j_{H^+} is the current density of H^+ reduction. We assumed the current density of H^+ reduction showed proportional relations with H^+ concentration at OHP and exponential relations with the potential of cathode:

$$j_{H^+} = -A c_{H^+} \exp\left(-\frac{\alpha F}{RT} \varphi_{\text{cathode}}\right) \quad (\text{Eq. 18})$$

In Stern layer, the Poisson equation is given by:

$$\frac{d}{dx}(\epsilon_0 \epsilon_r \frac{d\varphi}{dx}) = 0 \quad (\text{Eq. 19})$$

The left boundary condition in Stern layer is given as:

$$\varphi_{x=-0.4 \text{ nm}} = \varphi_{\text{cathode}} \quad (\text{Eq. 20})$$

A Neumann boundary condition was used at the OHP:

$$\left(\varepsilon_0 \varepsilon_r \frac{d\varphi}{dx}\right)_{x=0} = \varepsilon_0 \varepsilon_r \frac{\varphi_{x=0} - \varphi_{\text{cathode}}}{d_{\text{Stern}}} \quad (\text{Eq. 21})$$

4.3. Results and Validation

The simulation reproduced the features of HER at potentials more positive than the onset of the reduction of water (see Figure 5). In a K^+ -free solution, the current density of H^+ reduction increased without any limitation as the potential went cathodic. In a K^+ -containing solution, a plateau with a limiting current appeared. The simulation is verified by the experimental measurement under the same condition, shown in Figure 6. [7]

Figures 7a and 7b show the profiles of potential and electric field with and without K^+ ions. The existence of K^+ ions led to a stronger electric field in the Stern layer and a weaker electric field at >2 nm away from the cathode. In K^+ -containing medium, due to the competitive adsorption of hydrated K^+ ions against H^+ ions at OHP, a chemically inert hydrated K^+ layer formed at OHP and shielded the electric field from cathode in a long potential window. Thus, the migration of H^+ ions was significantly suppressed. [7]

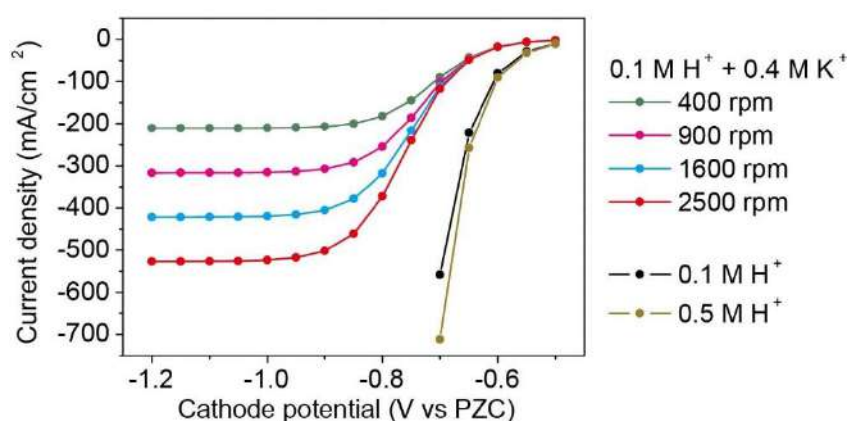


Figure 5. Simulated HER current density of Au electrode. 0.1 M HOTf + 0.4 M KOTf (green, pink, blue and red curves were simulated with the rotating speed of 400, 900, 1600, and 2500 rpm, respectively), 0.1 M HOTf (black, 400 rpm) and 0.5 M HOTf (brown, 400 rpm). [7]

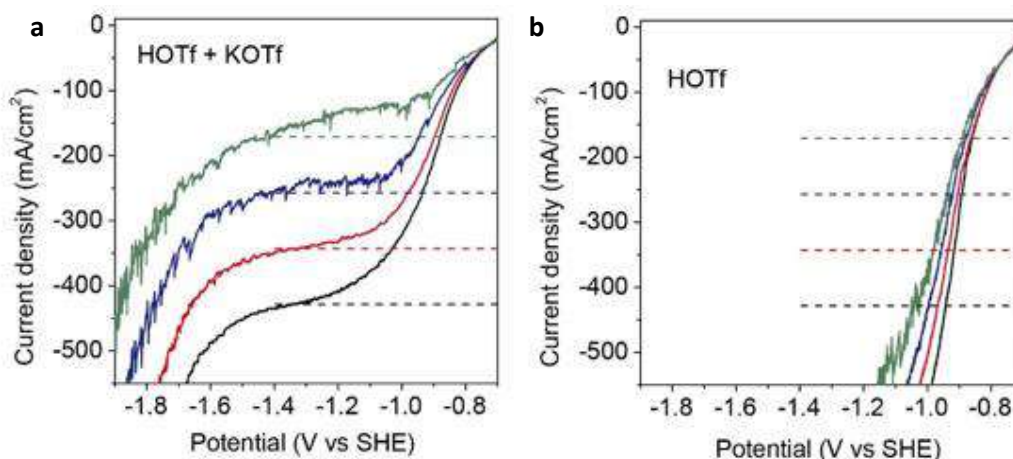


Figure 6. Current density curves of HER by SnO_2/C on RDE in a) 0.1 M HOTf + 0.4 M KOTf and b) 0.1 M HOTf. All electrolyte solutions were saturated with N_2 . Rotating speed: 400 rpm (green), 900 rpm (blue), 1600 rpm (red) and 2500 rpm (black). The horizontal dashed lines of each colour indicate the limiting diffusion current densities of the reduction of hydronium ions calculated according to Levich equation at the corresponding rotating speeds. [7]

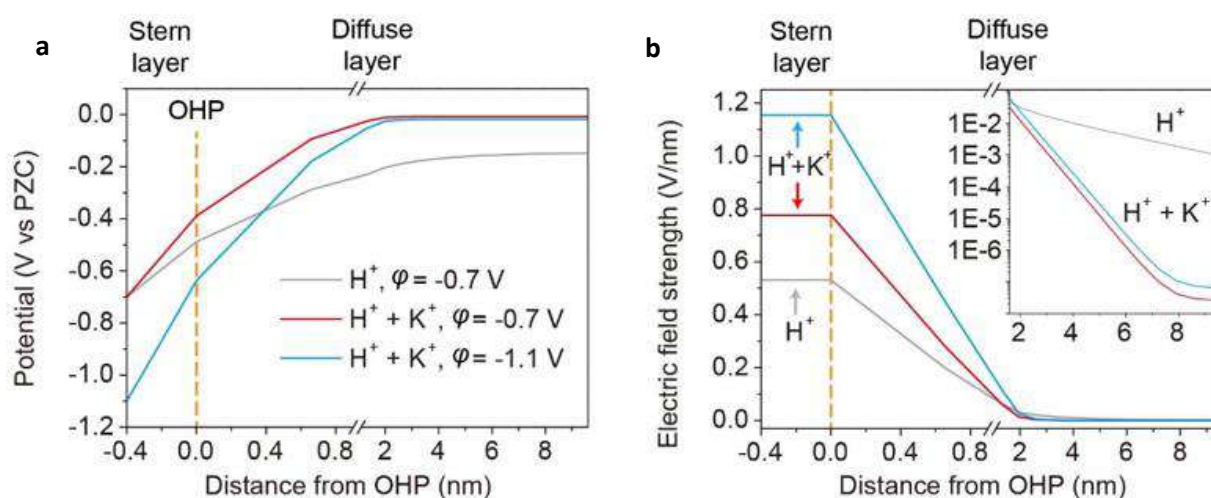


Figure 7. Cation effects on electric field distribution. a) Simulated potential and b) electric field strength along the Stern and diffuse/diffusion layer. The direction of electric field was towards the cathode. The surface of electrode was at $x = -0.4$ nm. The orange dashed lines at $x = 0$ nm represent OHP. Gray curves show the profiles of 0.1 M HOTf with the electrode potential of -0.7 V vs PZC. Red and blue curves show the profiles of 0.1 M HOTf + 0.4 M KOTf with the electrode potential of -0.7 V and -1.1 V vs PZC, respectively. The rotating speed was 400 rpm in the simulation. At -1.1 V vs PZC, the HER current density reached the plateau. The inset of panel b) shows the magnification of the electric field strength profile between 1.6 nm and 9.6 nm. [7]

5 INCLUSION OF PRODUCT ADSORPTION-DESORPTION PHENOMENA

In most models for CO_2 electrochemical reduction, the mass transport of products is only considered through the thermodynamics of their back reaction toward the reactant (in the anodic term of the Butler-Volmer like expression) or through the effect of bubble formation and detachment dynamics. [8] Because the experiments are usually performed at a non-negligible overpotential, the backward reaction is usually not expected to be present in a significant extent. Nevertheless, product could interfere with cathode performances through the thermodynamics of their adsorption-desorption on the surface, especially in the case of a highly coordinating molecule such as carbon monoxide (CO). Herein we have followed a procedure to quantify and adapt the current density expression (Eqs. 5 and 6) with the CO local concentrations.

5.1. Methodology

In order to avoid interference of gas evolution on convection and diffusion boundary layer model, we relied on experimental data obtained at an inverted rotating disk electrode (iRDE). [9] Such a setup allows for the gas bubbles to leave the surface easily and it was shown that the forced convection established by Levich [10] was still valid in the case of a gas evolution reaction (namely HER) up to 8 mA cm^{-2} . When they applied the same setup to CO_2 electrochemical reduction at a silver electrode coupled with an online gas chromatography (GC), they were able to plot both partial current densities as a function of the potential (Fig. 8).

In such an experiment, the H_2 production is expected to follow a Butler-Volmer like profile (exponential dependence on potential and linear dependence on reactants). At -1.8V vs. Ag/AgCl, the oxidation of H_2 is thermodynamically not favored so that the anodic back reaction is neglected. However, since the reactant is water (H^+ consumption is limited to a really small current that can be observed from -1.1 to -1.5V vs. Ag/AgCl), the dependence on reactant activity should be minimal so the current to potential profile (red trace) should be almost purely exponential. Instead, we observe an inhibition of HER reaction as CO takes off. This observation suggests an inhibition effect by the products. In a first approximation, we consider a Langmuir adsorption-desorption behavior of CO on the surface and investigate the effect of such a behavior and current intensity.

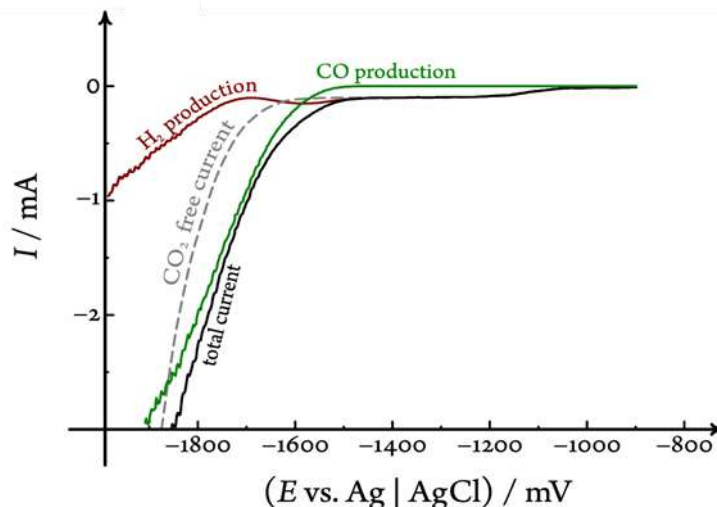


Figure 8. Linear Sweep Voltammetry at Ag iRDE ($\phi = 5\text{mm}$) in $0.1\text{ M K}_2\text{SO}_4$ saturated with CO_2 (pH 4.17), rotating speed of 625 rpm. In Red and Green respectively is the partial current of H_2 and CO deconvoluted thanks to the online GC. In gray is the H_2 current recorded in the same electrolyte under Ar. Reproduced from Ref [9].

5.2. Governing equations

5.1.1 Model geometry & boundary conditions

Due to the axial symmetry of the problem, the domain of the model is a rectangle considered in a cylindrical coordinate system (see Figure 9).

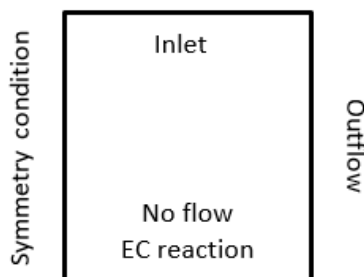


Figure 9. Geometry of the model domain and boundary conditions.

5.1.2 Homogeneous Convection-diffusion-reaction equation

In this model, migration is not (yet) implemented. The solution of the Navier-Stokes equations in this simplified 2D model domain describing the RDE can be analytically described:

$$v_z = -0.51\omega^{\frac{3}{2}}\nu^{-\frac{1}{2}}z^2 \quad (\text{Eq. 22})$$

$$v_r = 0.51\omega^{\frac{3}{2}}\nu^{-\frac{1}{2}}rz \quad (\text{Eq. 23})$$

The convection-diffusion-reaction equation (Eq. 17) is then solved for using the same parameters as in Section 2.2 for the homogeneous reaction terms and the diffusion coefficient values.

$$\frac{\partial c_i}{\partial t} = D\nabla c_i - \nabla(\mathbf{v}c_i) + R_i \quad (\text{Eq. 24})$$

5.1.3 CO adsorption-desorption model

We considered a Langmuir model for the adsorption-desorption of carbon monoxide:

$$K_1 [\text{CO}]_{\text{aq}} \Gamma_{\text{free active site}} = k_2 \Gamma_{\text{CO}} \quad (\text{Eq. 25})$$

$$\theta_{\text{free active site}} = \frac{\Gamma_{\text{free active site}}}{(\Gamma_{\text{CO}} + \Gamma_{\text{free active site}})} = \frac{1}{1 + K [\text{CO}]_{\text{aq}}} \quad (\text{Eq. 26})$$

Where Γ_i is the surface concentration of species i , $\theta_{\text{free active site}}$ is the proportion of active sites that is not occupied by carbon monoxide adsorbate, $[\text{CO}]_{\text{aq}}$ is the local concentration of carbon monoxide at the electrode/electrolyte interface and K is the equilibrium constant equal to k_1/k_2 .

5.1.4 Heterogeneous electrochemical reaction

The electrochemical reaction considered here are the same as in Section 2.2 but they are corrected for the lower amount of available active sites. Taking the assumption that both CO and HER current are proportional to the number of active sites, we obtain:

$$j_{\text{CO}} = j_{0,\text{CO}} \left(-\frac{c_{\text{CO}_2}}{c_{\text{CO}_2,0}} \exp\left(-\frac{\alpha_{\text{c,CO}}F\eta}{RT}\right) \right) \frac{1}{1+K[\text{CO}]_{\text{aq}}} \quad (\text{Eq. 27})$$

$$j_{\text{H}_2} = j_{0,\text{H}_2} \left(-\exp\left(-\frac{\alpha_{\text{c,H}_2}F\eta}{RT}\right) \right) \frac{1}{1+K[\text{CO}]_{\text{aq}}} \quad (\text{Eq. 28})$$

5.3. Validation

Thanks to the gray curve under Ag in Fig. 8, we first fit the HER curve in the absence of CO. We then use the same fit for HER but consider CO co-adsorption, to fit the remaining parameters (Table 4) to obtain a validation between experiments and model (see Figure 10).

The consideration of CO adsorption on silver electrode enabled to capture the behavior of H_2 production current during CO_2RR . Based on this first observation the model can be further refined taking into consideration the evolution of K value as a function of the pH, electrolyte and potential, and the competitive adsorption of CO with CO_2 . The migration effect described in section 3 can also be added.

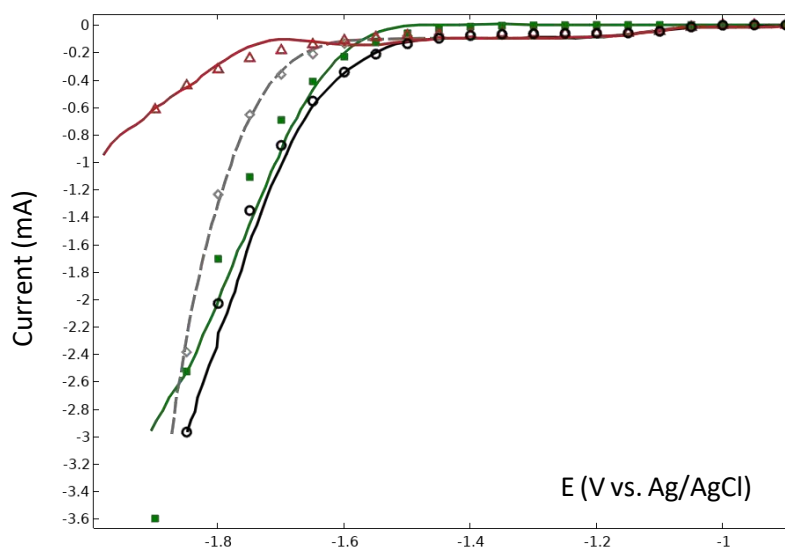


Figure 10. Identical to Figure 8 but with the computed partial current in colored marks.

Table 4. Empirical parameters fitted to the experimental data of a planar Ag RDE on the basis of our model and ref. [9]

i_{0,H_2} [mA cm ⁻²]	$i_{0,\text{CO}}$ [mA cm ⁻²]	β_{H_2}	β_{CO}	K [mM] ⁻¹
$1.8 \cdot 10^{-4}$	$7.5 \cdot 10^{-8}$	0.35	0.42	0.6

6 TOMOGRAPHY-BASED MODELING

A methodology for the morphological and transport characterization of materials with complex morphology was developed. The nano-tomography acquisition and segmentation procedure has been detailed in Deliverable 7.1, in addition to preliminary morphological characterization. In short, the workflow starts with a physical sample; after

the appropriate sample preparation the material is characterized through FIB-SEM tomography and an image processing procedure allows to obtain a digitalized 3D structure. The structure then undergoes in depth morphological characterization; subsequently it can be meshed and used in pore-scale simulations. The following results focus on the morphological characterization of three representative samples from SELECTCO2 partners.

6.1. Methodology

The focused ion beam – scanning electron microscopy (FIB-SEM) nanotomography is a destructive advanced characterization technique that allows for digitally reconstruction of a material with a resolution of up to 4 nm in the three dimensions. It makes use of two beams: a focused ion beam perpendicular to the sample mills the material of interest, previously embedded in epoxy, exposing new slices that are imaged thanks to a scanning electron microscopy column placed in front of the cross-section. A series of greyscale images is collected while the material is progressively milled, and a segmentation process allows for quantitative reconstruction of a 3D volume. An aggressive and a conservative segmentation are performed as well in order to obtain a confidence interval for segmentation and morphological characterization.

Three samples from SELECTCO2 partners were characterized as such: the samples are all a catalyst layer for CO₂ reduction deposited on gas diffusion layers (GDLs), but their chemical composition and their morphology vary significantly. The first sample was produced at the Technical University of Denmark (DTU) and consists of Cu sputtered on DeNora DN908 GDL; the second sample was produced at Delft University of Technology (TUD) and consists again of sputtered Cu but the support is a Sigracet 38BC GDL; finally, the third sample is a pyrolyzed Ni-based MOF deposited on DeNora DN908 GDL produced at Technical University Berlin (TUB). 3D rendering of the three representative samples are shown in Figure 11.

It is possible to obtain several pieces of quantitative information from the digitalized structures. Firstly, some simple structural descriptors are calculated:

- The volume of the solid is obtained simply by counting the number of voxels assigned to the solid phase and considering the resolution of the images.
- The interface area of a material is obtained with the MATLAB function “isosurface” (marching cubes algorithm). It is important to point out that the area calculated like this is the total interface of the material, which is not necessarily the area in contact with the electrolyte in the operating device. Furthermore, the obtained value is a lower limit to the real area of the sample, because the calculation is limited by the FIB-SEM resolution (4 nm). Roughness at smaller scale, which is important for chemical reactivity, is not quantified.
- The connected volume is the percentage of volume that is connected in one single component. By means of a flood-fill algorithm all the volume components are labelled.

Furthermore, the distribution of the material is studied by plotting the volume fraction profile and the characteristic volume of particles is characterized thanks to a morphological operation called opening. Finally, the anisotropy is studied by calculating the chord length distribution in the sample.

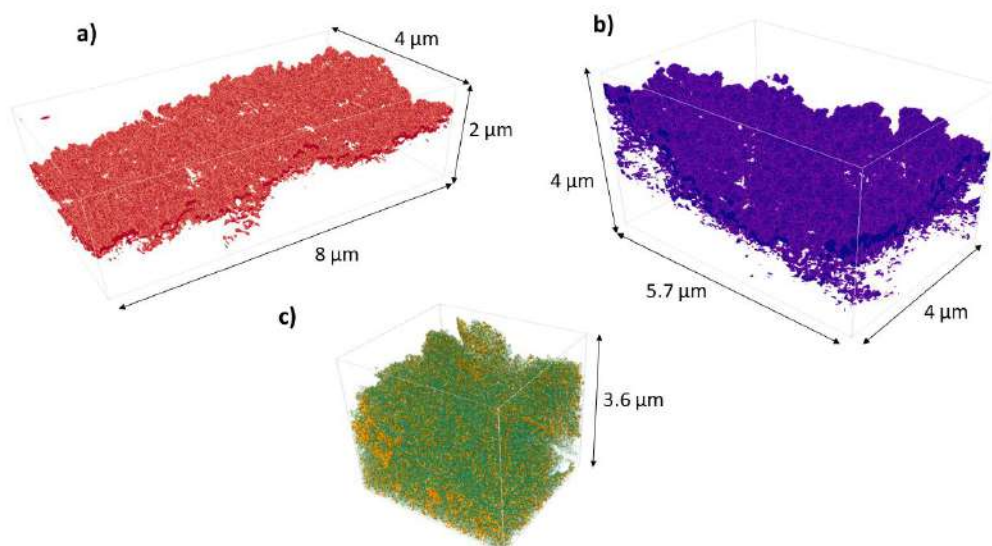


Figure 11. Segmented samples from a) TU Delft (Cu sputtered on Sigracet 38BC GDL); b) DTU (Cu sputtered on DeNora DN908 GDL) and c) TU Berlin (pyrolyzed Ni-based MOF on DeNora DN908 GDL). a) depicts the full corresponding catalyst layers, b) and c) are subsamples of the corresponding catalyst layers. The 3D images are produced with the open-source software Tomviz.

The reconstructed structure of the catalyst layers can be used as geometrical domain in pore-scale modelling in order to extract some relevant physical parameters to consider in the device-scale model. Before solving pore-scale simulations, two steps are necessary: extraction of a representative volume element (RVE) and meshing of the structure. The RVE is a subvolume of a given size that includes all the characteristic geometrical features of the considered sample. Since the physical properties depend on the structure of the material, it is assumed that a subvolume which correctly captures the main features of a structure will have a representative physical behaviour. The dimensions of the RVE should be big enough, so that all the characteristic morphologies of the structure are included, but small enough so that it will be possible to solve pore-scale simulations without having to face the problems of an excessive computational complexity. For the TUD and DTU samples, the full thickness of the sample is always considered when choosing the RVE, in order to include fully the catalyst layer, and the yz -plane is randomly sampled to select the subvolumes. In particular, subvolumes with edge from 200 nm to 800 nm will be considered. In the case of TUB sample, it was not possible to characterize the full catalyst layer as it was thicker than 8 μm (more details in the following section), so an arbitrarily large volume (better if isotropic, i.e. a cube) can be considered and the three dimensions can be randomly sampled in order to look for a RVE. Again, edges from 200 nm to 800 nm will be considered. In order to choose the appropriate RVE among the selected set of subvolumes of a given dimension, their two points correlation of is calculated, as well as the average correlation, which is taken to correspond to the sample two points correlation. The sample with two points correlation closer to average is selected as the RVE. The solid-solid two points correlation is calculated knowing that its Discrete Fourier Transform (DFT) is the DFT of the structure multiplied (element-wise product) by itself, and normalised by the volume. The two-point correlation is then simply obtained by inverse DFT.

Once the RVE is selected, the phase of interest for the following computational studies (solid or void) must be meshed. The meshing step is critical for the success of a pore-scale simulation and more in general of any finite element or finite volume simulation, and must include a mesh study step in order to ensure the convergence of the solution and its independency on the number of considered mesh elements. The mesh study is usually carried on a small subsample, which doesn't necessarily need to be representative. The meshing is performed with the open source software snappyHexMesh, available in the OpenFOAM package, and consists of several phases: first a structured hexahedral mesh generator builds a grid around the sample; this is followed by a castellation step, which refines the grid around the surface of the structure, a snapping step makes the nodes adhere to the surface and finally an optional layering step allows to create refined areas near the surface. The result is an unstructured hexahedral mesh; the main tuning parameters are the number of elements in the initial grid and the number of refinements in the castellation step.

The mesh can be used in pore-scale simulations in order to extract relevant physical parameters. The methodology is applicable to all samples; it was established for what concerns the calculation of effective diffusivity of different species in liquid and gas, as well as for the calculation of effective permeability, and it will be expanded to include calculations on effective conductivity in the solid phase and, possibly, effective heat transfer parameters.

To calculate the transport properties in dilute solution, the governing equations are given as

$$\nabla \cdot J_i = 0 \quad (\text{Eq. 29})$$

$$J_i = -\rho D_i \nabla w_i \quad (\text{Eq. 30})$$

where w_i is the volume fraction of the species i . The simulation region includes the porous structure and an inlet and outlet region as schematically depicted in Figure 12. These regions allow for the flow to develop before and after passing through the porous structure. The governing equations are solved in the fluid phase only.

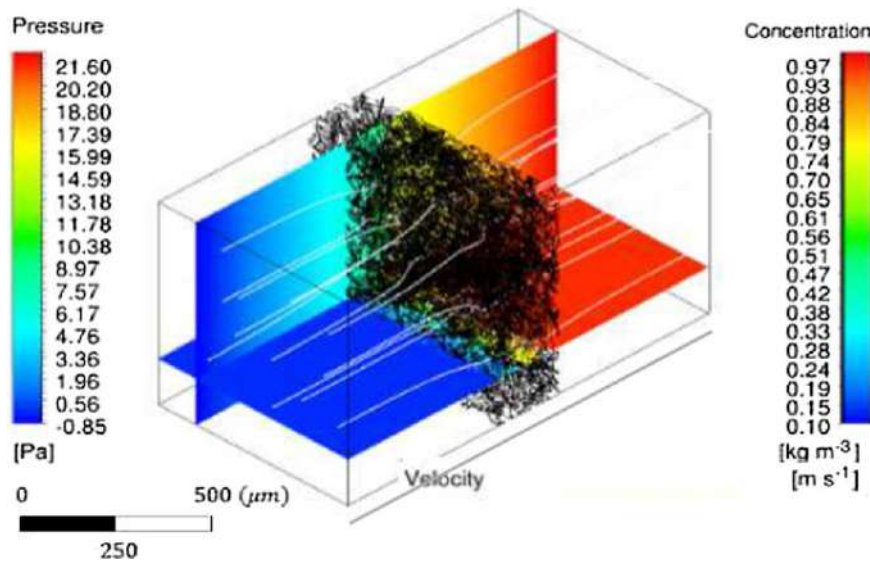


Figure 12. Schematic demonstration of the pore level transport simulation region and the resolved concentration and pressure field, and the stream lines. [11] The concentration gradient is established between two sides of the channel. In the middle, the species transport through the porous structure. Similar for the pressure gradient.

The solid boundary condition is a no flux boundary, since the species cannot diffuse into the catalyst. Two different concentrations are given as a boundary condition at the two extremes of the geometrical domain, and a concentration gradient is established. In the middle, the species diffuse through the porous structure. We set steady state conditions and no reaction term. The effective diffusivity can then be calculated based on:

$$D_{i,\text{eff}} = -\frac{J_i L}{\rho (w_2 - w_1)} \quad (\text{Eq. 31})$$

Similarly, the governing equation is applied also to the concentrated species transport (Eqs. 32 to 34) with the same boundary conditions setup, and the corresponding effective diffusivity can be obtained.

$$\nabla \cdot J_i = 0 \quad (\text{Eq. 32})$$

$$J_i = -\rho D_{i,m} \nabla w_i \quad (\text{Eq. 33})$$

$$D_{i,m} = \frac{1 - x_i}{\sum_{j \neq i} \left(\frac{x_j}{D_{ij}} \right)} \quad (\text{Eq. 34})$$

The effective permeability K_{eff} is obtained by solving the Navier-Stokes equations for a steady, laminar flux. This was done in the same model domain (Figure 12) but with an inflow velocity and outlet pressure as boundaries. The calculated pressure difference can then be used to calculate the effective permeability utilizing Darcy's law:

$$K_{\text{eff}} = -\frac{u \mu L}{(p_2 - p_1)} \quad (\text{Eq. 35})$$

L is the thickness of the porous layer; while u is the instantaneous flow rate and μ is the viscosity.

All the pore-scale problems are solved with Ansys Fluent, a commercial solver based on the finite volume method.

6.2. Sample characterization

Information about the characterized samples is gathered in Table 5.

Table 5. Characterization concerning the acquired samples. The samples are named as their institution of origin. “Picture dimensions” refers to the image taken with the SEM beam and “depth” refers to the depth of the milling with respect to the first image in the series and is related to the number of acquired images (number of images x resolution).

Sample	Composition	Resolution (nm)	Picture dimensions (μm^2)	Depth (μm)	Total volume (μm^3)
TU Delft	Cu sputtered on Sigracet 38BC GDL	4	8.2 x 8.5	4.6	321.3
DTU	Cu sputtered on DeNora DN908 GDL	4	9.9 x 7.1	7.6	532.5
TUB	Pyrolyzed Ni-based MOF on DeNora DN908 GDL	4	7.9 x 8	5.9	369.7

TU Delft and DTU catalyst layers were fully segmented. The TUB catalyst layer was thicker than $8 \mu\text{m}$ (it was not possible to mill the material further) and the sample was difficult to segment as it was subject to charging during the scan, which caused inhomogeneous contrast throughout the images. It was necessary to manually correct some images and to discharge some others, so that the final volume of the reconstructed sample was $7.9 \times 5.9 \times 5.0 \mu\text{m}^3$, or $230 \mu\text{m}^3$. Furthermore, the material includes two phases: the pyrolyzed MOF and some Ni nanoparticles (Ni NPs) formed as bi-product. Both phases were segmented and subjected to quantitative analysis.

6.3. Results

The TUD sample has a total volume of $6.1 \pm 0.6 \mu\text{m}^3$. The volume normalized with respect to the flat area is a quantity that can be compared among different samples; the flat area is simply the length and width of the total sampled volume for a given material. The normalized volume for TUD sample is $0.16 \pm 0.02 \mu\text{m}^3/\mu\text{m}^2$. The total interface area is calculated as well and corresponds to $297 \pm 17 \mu\text{m}^2$. To compare the characteristic surface of every sample, the surface is normalized with respect to the flat area. This quantity is often referred to as roughness factor and corresponds to 7.9 ± 0.5 for TUD sample. Again, the obtained value is a lower limit to the real value due to the 4 nm resolution limit. $97.31 \pm 0.06 \%$ of the solid is connected in this sample.

DTU sample has a total volume of $22 \pm 2 \mu\text{m}^3$, and a normalized volume of $0.30 \pm 0.02 \mu\text{m}^3/\mu\text{m}^2$. The total interface area for this sample is $1131 \pm 61 \mu\text{m}^2$, and the roughness factor is 15.0 ± 0.8 . $92 \pm 1 \%$ of the solid is connected.

In the case of TUB sample, the catalyst layer is thicker than $8 \mu\text{m}$, therefore it would be meaningless to normalize quantities with respect to the flat area. The pyrolyzed MOF total volume in the sample is $108.3 \pm 9.5 \mu\text{m}^3$, with a volume fraction of 0.450 ± 0.043 ; $99.84 \pm 0.09 \%$ of the solid and $99.9 \pm 0.1 \%$ of the void are connected. The surface was not calculated, as in case of MOFs the nanoporosities of dimension below the resolution limit are extremely relevant for chemical and physical properties. The sample also contains $13.0 \pm 1.6 \mu\text{m}^3$ of Ni NPs, with a volume fraction of 0.056 ± 0.007 . For all samples, also the volume fraction profile was calculated (see deliverable 7.1).

Opening is a morphological operation corresponding to an erosion followed by a dilation. The results of such operation is that all the roughnesses and particles smaller than the given structuring element (SE) are eliminated. Opening is performed with a structuring element of increasing diameter d and the volume fraction φ is calculated at each step, until it goes to zero. The cumulative opening size distribution $F(d)$ is calculated.

$$1 - F(d) = \frac{\phi(d)}{\phi_0} \quad (\text{Eq. 36})$$

The derivative of $F(d)$, $f(d)=F'(d)$, is the size distribution. From this distribution it is possible to obtain the average diameter of particles in the sample.

$$d_{mean} = \frac{\sum_{d_{min}}^{d_{max}} d \cdot f(d)}{\sum_{d_{min}}^{d_{max}} f(d)} \quad (\text{Eq. 37})$$

Figure 13 shows the distribution functions of the three samples.

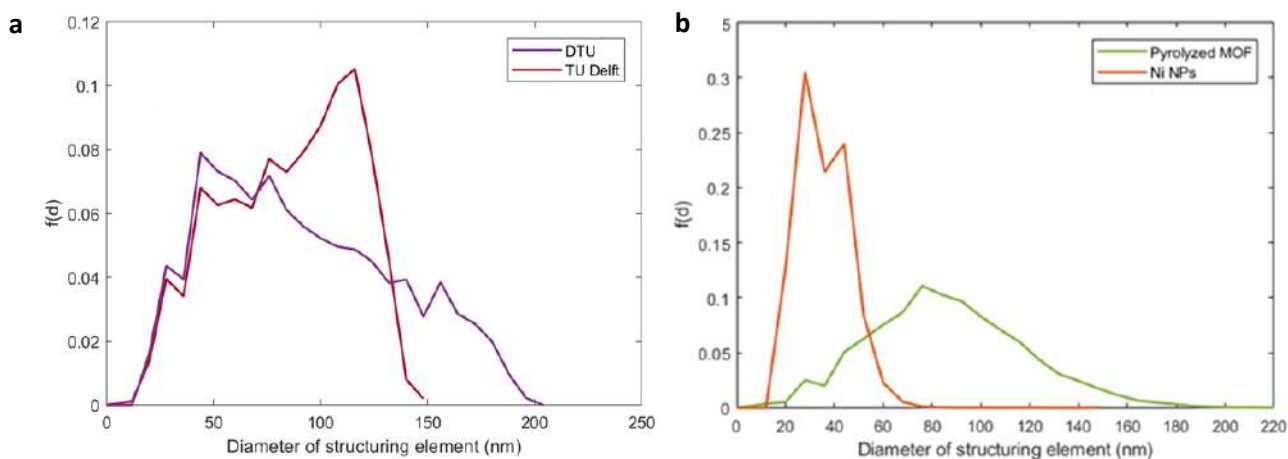


Figure 13. a) Size distribution of DTU and TUD samples and b) size distribution of pyrolyzed MOF and Ni NPs of TUB sample.

The diameter of the structuring element for which there is more variation in the volume fraction, which is the most represented diameter in the sample, corresponding to the maximum value of $f(d)$, in DTU and TU Delft sample is different – around 50 nm for TUD and around 120 nm for DTU. It can also be observed how the characteristic diameter of particles composing the DTU sample span on a larger interval (between 10 nm and 190 nm) while the diameters for TUD sample span between 10 and 150 nm, with diameters between 90 nm and 120 nm particularly represented. The average diameters for the two samples are close: for TU Delft, the mean diameter is $d_{mean}=85 \pm 3$ nm; while for DTU $d_{mean}=92 \pm 2$ nm. The results obtained in the opening size distribution can be considered as a confirmation of the fact that the DTU catalyst layer is more morphologically complex, with the most represented diameter being around 50 nm and a relevant amount of particles with diameters between 150 nm and 190 nm.

The pyrolyzed MOF has a most represented diameter of around 80 nm and a very wide distribution of particles sizes in its structure. The average diameter corresponds to 95 ± 6 nm. In the case of Ni NPs, the most represented diameter is about 25 nm, and the maximum diameter is less than 80 nm. The average diameter is 43.6 ± 0.9 nm. One additional morphological characterization parameter is given by the chord length distribution. It is calculated by measuring the length of the chords starting at one void-solid interface until the following solid-void interface along the given direction (x , y or z). The difference in chord length distribution in the 3 dimensions gives an indication of the anisotropy of the sample. The anisotropy is expected in such kind of catalyst layers along the x -axis, while isotropy is expected in the yz -plane. The milling of the material during FIB-SEM nanotomography proceeds along the z -direction, while the xy -plane is the one that is imaged via SEM. Figure 14 shows the chord length distribution for TUD and DTU samples, together with the reference system and the position of imaging planes in the tomography. The chord length distributions show a similar trend of the two samples along the y - and z -directions, which also confirms the good quality of the milling at the experimental stage, but in the x -direction the chord length of the TU Delft samples are on average significantly shorter. Again, an explanation for this could be that the TU Delft sample is flatter and less morphologically complex than the DTU sample.

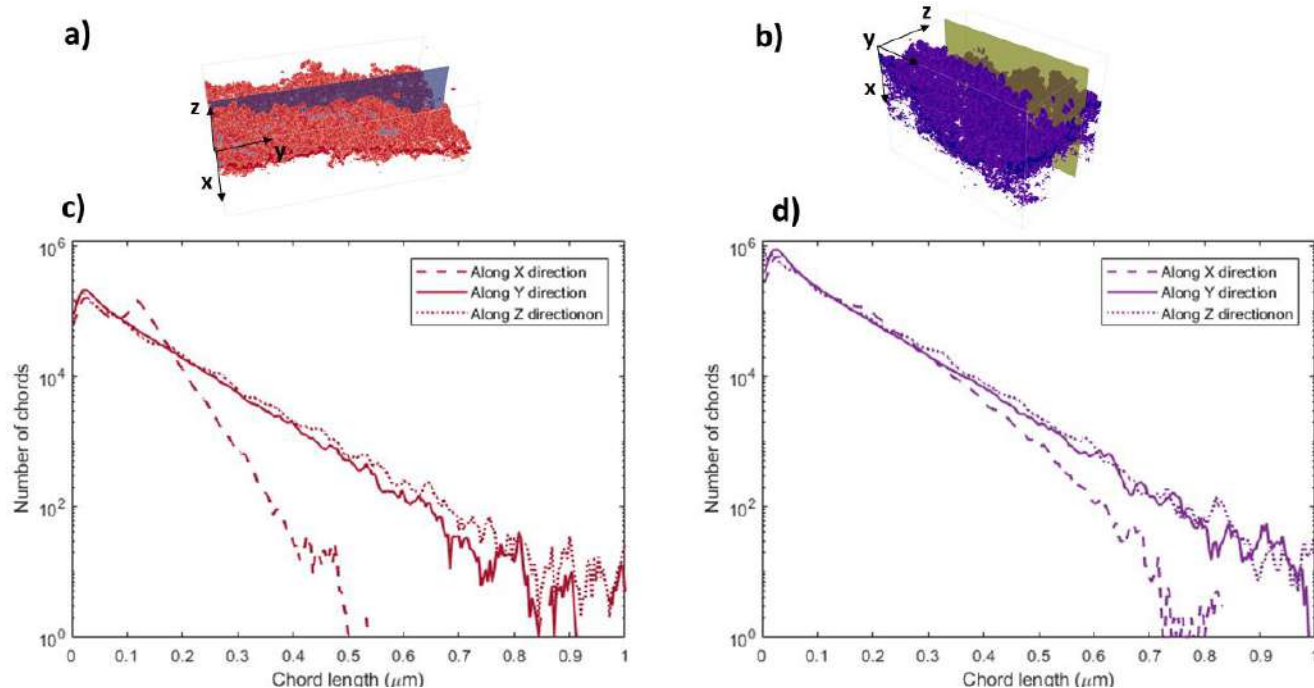


Figure 14. a) and b): 3D representation of TU Delft and DTU samples respectively, together with the adopted reference system and the position of one imaging plane. Milling is performed along the z direction. c) and d): chord length distribution along x-, y- and z-planes of TU Delft and DTU samples, respectively.

Concerning the pyrolyzed MOF chord length distribution in Figure 15, the distributions along the y- and z-directions show a similar trend, confirming again the good quality of the milling at the experimental stage, while in the x-direction the chord lengths are shorter. The Ni NPs are characterized, as expected, by short chords and an isotropic behaviour.

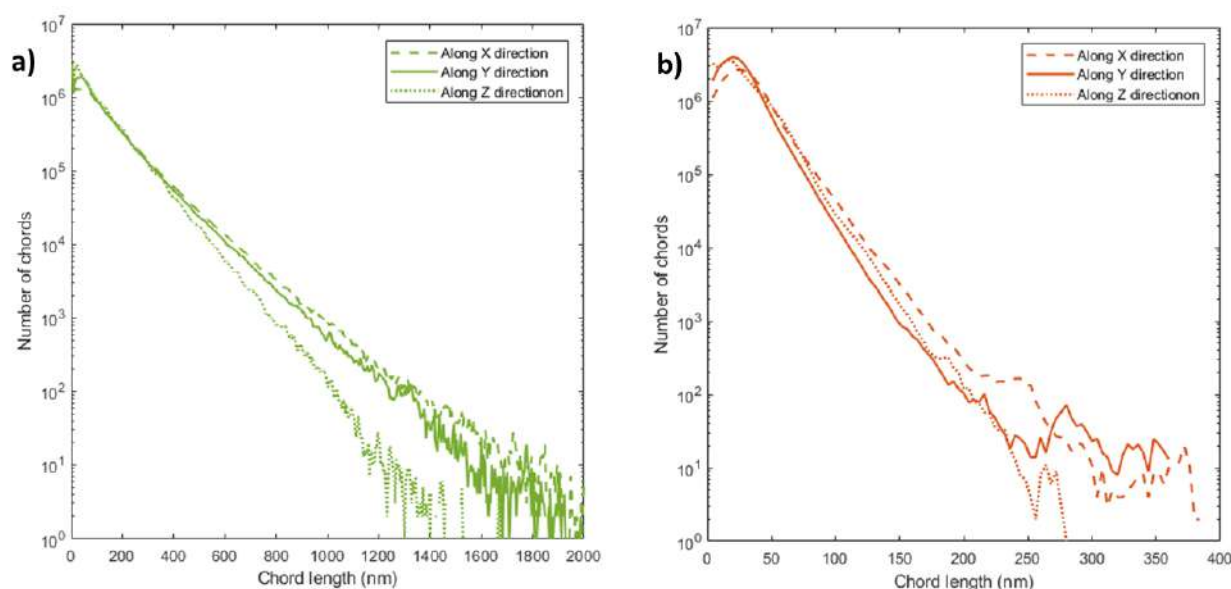


Figure 15. chord length distribution along x, y and z planes of a) pyrolyzed MOF and b) Ni NPs from the TUB sample.

Concerning pore-scale simulations for the characterization of the transport, the established methodology is valid for all the characterized samples, but the search for a RVE, the mesh study and the final meshing of the structures are time-consuming and computationally intensive tasks. A mesh study was performed on the structure of a GDL from DeNora (DN908) acquired via X-ray tomography (see Deliverable 5.3), while the meshing of the full structure

has proved to be particularly challenging for the high number of refinements needed to accurately mesh its fine details.

Preliminary data are available concerning the effective diffusivity of different species in the GDL in Tables 6 and 7, obtained by solving Eq. 31. The data are not representative yet, but they are coherent with respect to values reported in the literature, obtained by both, experimental methods and analytical models (see also Deliverable 5.3).

Table 6. Diffusion coefficients and effective diffusion coefficients of ionic species dissolved in water. D values are taken from [3].

Species	K ⁺	H ⁺	OH ⁻	HCO ₃ ⁻	CO ₃ ²⁻	CO _{2(aq)}
D (10 ⁻⁹ m ² /s)	1.957	9.311	5.293	1.185	0.923	1.910
D _{eff} (10 ⁻⁹ m ² /s)	0.0696	0.331	0.188	0.0421	0.0328	0.0679

Table 7. Diffusion coefficients and effective diffusion coefficients of different gaseous mixtures. D values are taken from [3].

Species	H ₂ /CO	H ₂ /N ₂	H ₂ /CO ₂	CO/N ₂	CO/CO ₂	N ₂ /CO ₂
D (10 ⁻⁵ m ² /s)	7.43	7.79	6.46	2.02	1.52	1.65
D _{eff} (10 ⁻⁵ m ² /s)	0.719	0.753	0.571	0.717	0.370	0.401

The effective permeability was calculated according to Eq. 35 and the preliminary results give K_{eff}=1.278 x 10⁻¹² m.

7 CONCLUSIONS

The pore level model constitute a first 3D CO₂ electrochemical reduction model resolved at the pore-level size. The model considered a reaction-diffusion equation in homogeneous phase coupled with a potential and local concentrations dependence on current density at the electrode/electrolyte interface. This first model has been validated with a comprehensive set of experimental data related to nanostructure silver electrode. Additionally, several features have been developed to further refine this mode such as a modeling of double layer capacitance and its effect on migration of charged species. This refined model revealed cation-induced modulation of electric field as the origin of important cation effects on selectivity. Additionally, we adapted the potential-current density relationship to consider not only the concentration of reactants but also the concentration of products and their adsorption-desorption kinetic effects on active site availability. To extend these models into a real electrode, we developed a nano-tomography based technique to analyze and segment in 3D a representative volume of real electrodes. Three samples were segmented and fully characterized with a reproducible and widely applicable methodology. The obtained structures will be meshed and will be considered in pore-scale simulations with the objective of extracting some relevant transport parameters to be used in device-scale modelling. The developed method allows for considering additional phenomena, for example, the charge transport in the solid.

8 REFERENCES

- [1] S. Suter et S. Haussener, « Optimizing mesostructured silver catalysts for selective carbon dioxide conversion into fuels », *Energy Environ. Sci.*, **12**, 1668-1678, 2019, doi: 10.1039/C9EE00656G
- [2] Y. Yoon, A. S. Hall, et Y. Surendranath, « Tuning of Silver Catalyst Mesostructure Promotes Selective Carbon Dioxide Conversion into Fuels », *Angewandte Chemie International Edition*, **55**, 15282-15286, 2016, doi: 10.1002/anie.201607942
- [3] L.-C. Weng, A. T. Bell, et A. Z. Weber, « Modeling gas-diffusion electrodes for CO₂ reduction », *Phys. Chem. Chem. Phys.*, **20**, 16973-16984, 2018, doi: 10.1039/C8CP01319E
- [4] Chu, S., Cui, Y. & Liu, N. The path towards sustainable energy. *Nat. Mater.* **16**, 16-22, (2017).
- [5] Verma, S. *et al.* Insights into the Low Overpotential Electroreduction of CO₂ to CO on a Supported Gold Catalyst in an Alkaline Flow Electrolyzer. *ACS Energy Lett.* **3**, 193-198, (2018).

- [6] Dinh, C.-T., García de Arquer, F. P., Sinton, D. & Sargent, E. H. High Rate, Selective, and Stable Electroreduction of CO₂ to CO in Basic and Neutral Media. *ACS Energy Lett.* **3**, 2835-2840, (2018).
- [7] Gu J, Liu S, Ni W, Ren W, Haussener S, Hu X. Modulating Electric Field Distribution by Alkali Cations for CO₂ Electroreduction in Strongly Acidic Medium. ChemRxiv. Cambridge: Cambridge Open Engage.
- [8] T. Burdyny *et al.*, « Nanomorphology-Enhanced Gas-Evolution Intensifies CO₂ Reduction Electrochemistry », *ACS Sustainable Chem. Eng.*, **5**, 4031-4040, mai 2017, doi: 10.1021/acssuschemeng.7b00023
- [9] P. Moreno-García, N. Kovács, V. Grozovski, M. de J. Gálvez-Vázquez, S. Vesztergom, et P. Broekmann, « Toward CO₂ Electroreduction under Controlled Mass Flow Conditions: A Combined Inverted RDE and Gas Chromatography Approach », *Anal. Chem.*, **92**, 4301-4308, mars 2020, doi: 10.1021/acs.analchem.9b04999
- [10] V. G. Levich, *Physicochemical hydrodynamics*. Englewood Cliffs, N.J.: Prentice-Hall, 1962
- [11] S.M. Moosavi *et al.*, « Transport characteristics of saturated gas diffusion layers treated with hydrophobic coatings », *Chemical Engineering Science* **176**, 503-514, (2018).